

A LINE-SMEARED TREATMENT OF OPACITIES FOR THE SPECTRA AND LIGHT CURVES FROM MACRONOVAE

CHRISTOPHER J. FONTES¹, CHRIS L. FRYER^{1,2,3}, AIMEE L. HUNGERFORD¹, RYAN T. WOLLAEGER¹,
 STEPHAN ROSSWOG⁴, AND EDO BERGER⁵

¹Los Alamos National Laboratory, Los Alamos, NM 87545, USA

²Physics Department, University of Arizona, Tucson, AZ 85721, USA

³Physics and Astronomy Department, University of New Mexico, Albuquerque, NM 87131, USA

⁴Astronomy and Oskar Klein Centre, Stockholm University, AlbaNova, SE-10691 Stockholm, Sweden

⁵Harvard-Smithsonian Center for Astrophysics, 60 Garden Street, Cambridge, MA 02138, USA

Draft version September 8, 2018

ABSTRACT

Gravitational wave observations need accompanying electromagnetic signals to accurately determine the sky positions of the sources. The ejecta of neutron star mergers are expected to produce such electromagnetic transients, called macronovae. Characteristics of the ejecta include large velocity gradients and the presence of heavy r -process elements, which pose significant challenges to the accurate calculation of radiative opacities and radiation transport. For example, these opacities include a dense forest of bound-bound features arising from near-neutral lanthanide and actinide elements. Here we investigate the use of fine-structure, line-smeared opacities that preserve the integral of the opacity over frequency, which is an alternative approach to the expansion-opacity formalism. The use of area-preserving line profiles produces frequency-dependent opacities that are one to two orders of magnitude greater than those obtained with the use of expansion opacities in the Sobolev approximation. Opacities are calculated for four r -process elements (cerium, neodymium, samarium and uranium) using fully and semi-relativistic methods, as well as different amounts of configuration interaction in the atomic structure, in order to test the sensitivity of the emission to the underlying atomic physics. We determine the effect of these new opacities on simulated spectra and broad-band light curves by applying a multi-dimensional ray-trace method to the ejecta predicted from 3-dimensional merger calculations. With our substantially larger opacities the simulations yield slightly lower luminosities that peak in the mid-IR. These results suggest that those radioactively powered transients that are related to the very heaviest r -process material are more difficult to observe than previously believed.

Subject headings: gravitational waves — opacity — radiative transfer stars: neutron

1. INTRODUCTION

With the recent announcement of the first direct observation of gravitational waves (GW; Abbott et al. 2016a,b,c) the era of gravitational wave astronomy has begun. This discovery provides urgent motivation for a deeper understanding of the physics of the GW sources and their evolutionary paths. While the observed merger of two black holes is from a gravitational point of view the cleanest possible system, the lack of an accompanying electromagnetic (EM) signal¹ leaves us blind with respect to the astrophysical environment of the source. Although most detected GW sources are nowadays believed to be black hole binaries (Belczynski et al. 2010; Dominik et al. 2015), neutron star mergers (NSMs) are another major source of gravitational waves for which an EM signal is clearly expected. The short-term EM waves are predicted to occur in two forms: gamma-ray bursts (GRBs) (Eichler et al. 1989; Kouveliotou et al. 1993; Berger 2014) and dim, supernova-like events (Li & Paczyński 1998), sometimes referred to as macronovae (Kulkarni 2005) or kilonovae (Metzger et al. 2010). The GRBs are expected to be short-lived with a beamed signal, offering a relatively low probability of being observed (see, for example,

Fong et al. 2012; Berger et al. 2013; Fong et al. 2014; Grossman et al. 2014; Fong et al. 2015). On the other hand, macronovae², which are the focus of the present study, are predicted to generate relatively isotropic signals and therefore offer a major advantage for coincident observation with gravitational waves.

An understanding of the EM emission produced by macronovae requires detailed information and simulations, such as the composition, velocity structure and opacity of the ejecta, and the transport of radiation through this material. Theoretical investigations of these transients have undergone steady improvement in various respects, especially the characterization of the opacity, which we summarize here. Early light-curve estimates (Li & Paczyński 1998) were determined from a constant opacity, $0.2 \text{ cm}^2/\text{g}$, due to electron scattering. That well-known gray opacity value results from the Thomson-scattering opacity, $\kappa^T = 0.4(\bar{Z}/A) (\text{cm}^2/\text{g})$, under the assumption of fully ionized material, i.e. $\bar{Z} = Z$. Here, Z is the atomic number, A the atomic weight, \bar{Z} the mean ion charge, and $Z/A \approx 1/2$ for most elements. An improvement over this approach was to approximate the complex opacity of the r -process elements in the ejecta

¹ But see the recent controversy (Connaughton et al. 2016; Lyutikov 2016; Greiner et al. 2016) about a claimed EM counterpart.

² In this work, we favor the more generic term “macronova” over “kilonova” because simulated luminosities have moved progressively lower than the original estimate of 1,000 times that associated with a standard nova.

using bound-bound lines from iron, along with corrections to the ionization energies (Metzger et al. 2010).

Significantly improved opacities were subsequently obtained by the Mons group (Biémont et al. 1999; Quinet et al. 1999; Palmeri et al. 2000; Biémont et al. 2004; Quinet & Biémont 2004) using modern atomic structure calculations of neutral and near-neutral lanthanide species (i.e. the D.R.E.A.M. database). Their approach employs the least-squares fitting procedure in the Cowan code (Cowan 1981) in conjunction with a core-polarization potential to obtain spectroscopic quality radiative rates. However, this approach requires access to accurate level energies, which are not readily available for the large number of levels required to construct complete atomic models for macronova simulations. A more recent approach used *ab initio* atomic structure calculations of *r*-process elements in combination with the expansion-opacity approach (Sobolev 1960; Castor 1974; Karp et al. 1977) to produce detailed spectra and light curves (Kasen et al. 2013). The latter investigation included neodymium as a representative ejecta element, using realistic near-neutral ion species, rather than the assumption of full ionization. A complementary study was performed using opacities composed of all the *r*-process elements (Tanaka & Hotokezaka 2013). This progression in opacity improvements moved the prediction of peak emission to progressively longer wavelengths, with current best estimates going as low as the near-infrared band (Barnes & Kasen 2013). Recent modeling has taken into account these more realistic opacities to study various aspects of macronovae. For example, a more sophisticated treatment of the ejecta geometry has been considered in 3D hydrodynamic simulations (Rosswog et al. 2014; Grossman et al. 2014). This study used an enhanced gray opacity for the ejecta, $10 \text{ cm}^2/\text{g}$, and explored in a simple model the possibility of a second transient due to neutrino-driven winds with an opacity of $1 \text{ cm}^2/\text{g}$ to represent elements of intermediate mass between iron and the lanthanides. Such wind transients have been explored in more detail recently based on 3D hydrodynamical simulations (Perego et al. 2014; Martin et al. 2015).

The opacity of *r*-process ejecta in NSMs, however, remains a significant source of uncertainty in the simulation of macronova emission. A single ion stage for a lanthanide or actinide element can produce in excess of $\sim 10^8$ lines for the conditions of interest (see Section 2). While it is impossible to calculate all such lines with spectroscopic accuracy, the presence of large velocity gradients might allow simplifications in the opacity calculations. The expansion-opacity formalism developed to study Type Ia supernovae (Eastman & Pinto 1993; Fryer et al. 1999; Pinto & Eastman 2000; Kasen 2006, e.g.), is based on the argument that the opacity can be modeled by a finite number of distinct strong lines. If the photon is re-emitted at the same energy as it is absorbed, we can treat each line as a scattering center. The strong velocity gradients mean that, as this photon travels, the Doppler effect on its energy with respect to the rest frame of the matter shifts it off the line center, allowing it to once again transport until it is Doppler boosted into another line (Sobolev 1960; Castor 1974; Karp et al. 1977). Among the simplifying assumptions in this method are that the lines dominating the opacity

are sufficiently distinct, such that radiation transport for each line can be treated individually, and there is no line splitting, also known as fluorescence (i.e. no altering of the photon energy due to emission via a transition different from the absorbing one). In general, these assumptions do not hold for most supernova calculations. Where they are valid, perhaps for some wavelengths and times in type Ia supernovae (Pinto & Eastman 2000), this expansion opacity greatly simplifies the opacity calculations.

For the dense forest and complex structure of lines for the *r*-process elements, this expansion approximation may not be valid. Not only do these elements produce a dense cluster of lines in the optical and near infra-red bands (a single lanthanide or actinide element can produce one to two orders of magnitude more lines than iron or silicon), but the opacity is dominated by a broad set of elements, rather than a few. For example, in our NSMs, a significant number of lanthanide and actinide elements are predicted to be present in the ejecta (see Figure 1), which are expected to provide the dominant contribution to the opacity.

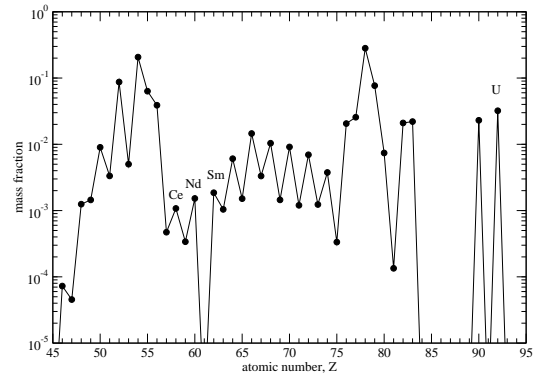


FIG. 1.— Predicted elemental abundances for the ejecta produced in a $1.4 + 1.4 M_{\odot}$ neutron star merger (Rosswog et al. 2014; Grossman et al. 2014). Labels are provided for the four elements considered in this work.

In earlier works, the process of fluorescence was found to be high and was included to modify to the expansion opacities in order to obtain improved agreement with observations for Type Ia supernovae (Pinto & Eastman 2000; Kasen 2006). Here, we investigate the possibility that fluorescence is sufficiently strong in the NSM ejecta to destroy the coherent scattering associated with multiple photon scatterings within a line. We explore such an approach by smearing the lines in a manner that conserves the total integral of the frequency-dependent opacity (Fontes et al. 2015a). For computational convenience we perform the smearing via a Doppler width in the Voigt line profile, choosing a characteristic value that is consistent with the spatial resolution employed in our light-curve simulations. Of course, Doppler broadening is formally associated with absorbers undergoing random motion, as opposed to the ordered, homologous expansion of the ejecta. Also, the Voigt profile is symmetric about the line center, while the opacity-expansion formalism combined with the homologous flow assumes that the photons undergo only redward shifts. Nevertheless, we expect our approach to take into account, in an average sense, the fact that a radial zone, which is characterized by a zone-centered velocity, actually encompasses

a range of velocities, with photons that are both redder and bluer relative to their energy at the zone center (see Section 4.1).

This line-smeared approach requires detailed opacity calculations for all lines and is computationally intensive, but it automatically takes into account the case of strong line splitting. Detailed atomic physics models are presented for three lanthanides and one actinide in Section 2: Ce ($Z = 58$), Nd ($Z = 60$), Sm ($Z = 62$) and U ($Z = 92$). We provide several different atomic physics models to assess the sensitivity of the opacities, light curves and spectra to the quality of the atomic data. Line-smeared opacities are presented for these four elements in Section 3. As expected, the resulting opacities are significantly enhanced (by one to two orders of magnitude) compared to those obtained via the Sobolev reduction employed in the opacity-expansion formalism.

In Section 4 we use a 2-dimensional ray-trace transport code to determine the effect of different variants of the opacity calculations on the spectra and broadband light curves from the ejecta of three merger models (Rosswog et al. 2014), mapping these 3-dimensional models assuming cylindrical symmetry. We summarize with a brief discussion of the implications of our results for observations.

2. ATOMIC PHYSICS CONSIDERATIONS

2.1. Computational Framework

In this work we use the Los Alamos suite of atomic physics and plasma modeling codes (see Fontes et al. 2015b and references therein) to generate the fundamental data and opacities needed to simulate the characteristics (time to peak, spectra, luminosities, decay times, etc.) associated with neutron star mergers. For a given element, a model is composed of the atomic structure (energies, wavefunctions and oscillator strengths) and photoionization cross sections. Both the fully and semi-relativistic capabilities of the suite are used in this work.

The fully relativistic (FR) approach is based on bound- and continuum-electron wavefunctions that are solutions of the Dirac equation, while the semi-relativistic (SR) approach uses solutions of the Schrödinger equation with relativistic corrections. A fully relativistic (FR) calculation begins with the RATS atomic structure code (Fontes et al. 2015b) using the Dirac-Fock-Slater method of Sampson and co-workers (Sampson et al. 2009). A semi-relativistic (SR) calculation begins with the CATS atomic structure code (Abdallah et al. 1988) using the Hartree-Fock method of Cowan (Cowan 1981). These calculations produce detailed, fine-structure data that include a complete description of configuration interaction for the specified list of configurations. Two variant, relativistic calculations are also considered that include incomplete amounts of configuration interaction (see Section 2.2). After the atomic structure calculations are complete, both the FR and SR methods use the GIPPER ionization code to obtain the relevant photoionization cross sections in the distorted-wave approximation. The photoionization data are used to generate the bound-free contribution to the opacity and are not expected to be too important for the present application, due to the range of relevant photon energies, but are included for completeness. Therefore, they are calculated

in the configuration-average approximation, rather than fine-structure detail, in order to minimize the computational time.

The atomic level populations are calculated with the ATOMIC code from the fundamental atomic data. The code can be used in either local thermodynamic equilibrium (LTE) or non-LTE mode (Magee et al. 2004; Hakel et al. 2006; Colgan et al. 2016; Fontes et al. 2016). The LTE approach was chosen for the present application, which requires only the atomic structure data in calculating the populations. At the relevant times, the ejecta densities are low enough that collective, or plasma, effects are not important and simple Saha-Boltzmann statistics is sufficient to produce accurate level populations. The populations are then combined with the oscillator strengths and photoionization cross sections in ATOMIC to obtain the opacities, which are constructed from the standard four contributions: bound-bound (b-b), bound-free (b-f), free-free (f-f) and scattering. Specific formulae for these contributions are readily available in various textbooks, such as Huebner & Barfield (2014). Here, we reproduce only the expression for the bound-bound contribution, as it is useful for the subsequent discussion of line-smeared opacities in Section 3:

$$\kappa_{\nu}^{\text{b-b}} = \frac{\pi e^2}{\rho m_e c} \sum_i N_i |f_i| L_{i,\nu}, \quad (1)$$

where ν is the photon energy, ρ is the mass density, N_i is the number density of the initial level in transition i , f_i is the oscillator strength describing the photo-excitation of transition i , and $L_{i,\nu}$ is the corresponding line profile function.

2.2. Baseline Atomic Models

As mentioned in Section 1, atomic models were created for four elements: Ce ($Z = 58$), Nd ($Z = 60$), Sm ($Z = 62$), and U ($Z = 92$). In order to obtain converged opacities for the range of temperatures and densities in our simulations, only the first four ion stages of each element were considered, similar to the choice made by Kasen et al. (2013). A list of configurations chosen for each element is provided in Table 1. Since Nd was used as a representative element in the recent study by Kasen et al. (2013), we chose an identical list of configurations for that element in order to make meaningful comparisons. As expected, the number of Nd levels is identical to those appearing in Table 1 of that earlier work.³ The number of lines is slightly higher in the present listing, possibly due to the retention of small oscillator strengths that do not affect the modeling in a significant way. We did some tests to include higher lying configurations, but found that the displayed list is sufficient to produce converged opacities due to the relatively low temperature and densities of the ejecta. Therefore, the configuration lists for the other elements were chosen in a similar fashion. The configurations for Ce II and Ce III are also identical to those chosen by Kasen et al. (2013). The number of levels and lines differ strongly in this case. We cross-checked the values between our FR

³ Based on this analysis, the $4f^4 6s^1 6p^1$ configuration appears to have been left out of Table 1 of Kasen et al. (2013).

TABLE 1

A list of configurations, number of fine-structure levels, and number of (electric dipole) absorption lines for the various ion stages considered in this work. A completely filled Xe core is assumed for Ce, Nd and Sm, while a filled Rn core is assumed for U.

Ion stage	Configurations	# of levels	# of lines
Ce I	$4f^2 6s^2$, $4f^1 5d^1 6s^2$, $4f^1 5d^2 6s^1$, $4f^1 5d^1 6s^1 6p^1$, $4f^2 5d^1 6s^1$, $4f^2 6s^1 6p^1$, $4f^1 5d^3$, $4f^1 6s^2 6p^1$, $4f^1 5d^2 6p^1$, $4f^2 5d^2$, $4f^2 5d^1 6p^1$	2,546	626,112
Ce II	$4f^2 6s^1$, $4f^2 5d^1$, $4f^2 6p^1$, $4f^1 5d^2$, $4f^1 6s^2$, $4f^1 5d^1 6s^1$, $4f^1 5d^1 6p^1$, $4f^1 6s^1 6p^1$, $5d^3$, $4f^3$	519	28,887
Ce III	$4f^2$, $4f^1 6s^1$, $4f^1 5d^1$, $4f^1 6p^1$, $5d^2$, $5d^1 6s^1$	62	452
Ce IV	$4f^1$, $6s^1$, $5d^1$, $6p^1$	7	8
Nd I	$4f^4 6s^2$, $4f^3 5d^1 6s^2$, $4f^4 5d^1 6s^1$, $4f^4 5d^2$, $4f^3 5d^1 6s^1 6p^1$, $4f^4 5d^1 6p^1$, $4f^4 6s^1 6p^1$	18,104	25,224,451
Nd II	$4f^4 6s^1$, $4f^4 5d^1$, $4f^4 6p^1$, $4f^3 5d^2$, $4f^3 5d^1 6s^1$, $4f^3 5d^1 6p^1$, $4f^3 6s^1 6p^1$	6,888	3,958,977
Nd III	$4f^4$, $4f^3 6s^1$, $4f^3 5d^1$, $4f^3 6p^1$, $4f^2 5d^2$, $4f^2 5d^1 6s^1$, $4f^1 5d^2 6s^1$	1,650	233,822
Nd IV	$4f^3$, $4f^2 6s^1$, $4f^2 5d^1$, $4f^2 6p^1$	241	5,784
Sm I	$4f^6 6s^2$, $4f^5 5d^1 6s^2$, $4f^6 5d^1 6s^1$, $4f^6 5d^2$, $4f^5 5d^1 6s^1 6p^1$, $4f^6 5d^1 6p^1$, $4f^6 6s^1 6p^1$	60,806	249,301,825
Sm II	$4f^6 6s^1$, $4f^6 5d^1$, $4f^6 6p^1$, $4f^5 5d^2$, $4f^5 5d^1 6s^1$, $4f^5 5d^1 6p^1$, $4f^5 6s^1 6p^1$	29,970	67,743,385
Sm III	$4f^6$, $4f^5 6s^1$, $4f^5 5d^1$, $4f^5 6p^1$, $4f^4 5d^2$, $4f^4 5d^1 6s^1$, $4f^3 5d^2 6s^1$	13,170	13,318,114
Sm IV	$4f^5$, $4f^4 6s^1$, $4f^4 5d^1$, $4f^4 6p^1$	1,994	320,633
U I	$5f^4 7s^2$, $5f^3 6d^1 7s^2$, $5f^4 6d^1 7s^1$, $5f^4 6d^2$, $5f^3 6d^1 7s^1 7p^1$, $5f^4 6d^1 7p^1$	16,882	20,948,831
U II	$5f^3 7s^2$, $5f^4 7s^1$, $5f^4 6d^1$, $5f^4 7p^1$, $5f^3 6d^2$, $5f^3 6d^1 7s^1$, $5f^3 6d^1 7p^1$, $5f^3 7s^1 7p^1$	6,929	4,016,742
U III	$5f^4$, $5f^3 7s^1$, $5f^3 6d^1$, $5f^3 7p^1$, $5f^2 6d^2$, $5f^2 6d^1 7s^1$, $5f^1 6d^2 7s^1$	1,650	233,822
U IV	$5f^4 7s^2$, $5f^3 6d^1 7s^2$, $5f^4 6d^1 7s^1$, $5f^4 6d^2$, $5f^3 6d^1 7s^1 7p^1$, $5f^4 6d^1 7p^1$	241	5,784

and SR calculations, which agree well, so those earlier values appear to be in error.

As a proxy for the quality of our atomic structure calculations, the ionization energies for the FR and SR models are presented in Table 2, along with the values from the NIST database (Kramida et al. 2015). The over-

TABLE 2

Ionization energies for the first three ion stages of each element considered in this work. Values are presented for the fully relativistic (FR) and semi-relativistic (SR) methods described in the text, as well as from the NIST database (Kramida et al. 2015).

Ion stage	Ionization energy (eV)		
	FR	SR	NIST
Ce I	4.91	5.24	5.54
Ce II	10.5	11.2	10.9
Ce III	18.0	19.6	20.2
Nd I	4.58	4.97	5.53
Nd II	10.9	11.1	10.7
Nd III	19.2	20.5	22.1
Sm I	4.83	5.33	5.64
Sm II	10.6	10.7	11.1
Sm III	20.3	21.6	23.4
U I	4.00	5.48	6.19
U II	12.1	11.7	11.6
U III	17.4	19.2	19.8

all agreement is good, with the worst comparisons occurring for the neutral ion stage (particularly for uranium), which is typically the most difficult to calculate due to the presence of more bound electrons and the need to accurately describe the correlation between

them. As expected, the SR values are more accurate than the FR values for these near-neutral ions for two reasons. First, the Hartree-Fock approach uses a better (non-local) description of the exchange interaction between the bound electrons than the Dirac-Fock-Slater method, which uses the Kohn-Sham local-exchange approximation (Kohn & Sham 1965; Sampson et al. 2009). Second, the SR approach uses semi-empirical scale factors to modify the radial integrals that appear in the configuration-interaction calculation (Cowan 1981). In any event, the inaccuracies in the ionization energies have been removed in both the FR and SR models of the present study by replacing the calculated values with those appearing in the NIST database. All level energies within an ion stage were shifted by the same amount when implementing this procedure. Of course, inaccuracies in the calculated ionization energies are reflected in the individual level energies as well, but the line positions are determined by taking the difference of energies within the same ion stage. So some beneficial cancellation is expected in this regard when systematic shifts are present within a given ion stage. The NIST ionization-energy correction was applied to all of the models considered in this work. An illustration of the ionization balance that is obtained with these improved energies is provided in Figure 2 for Nd at a mass density of $\rho = 10^{-13}$ g/cm³, corresponding to the ejecta density at ~ 1 day after the merger (see Figure 3 in Rosswog et al. 2014). This behavior is typical for all of the elements considered in this work.

2.3. Variant Models

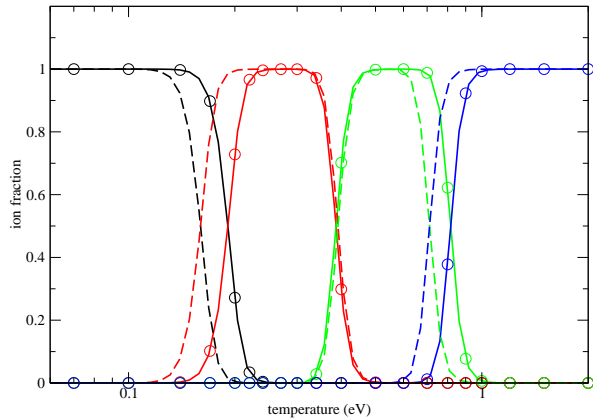


FIG. 2.— Ionization-stage fraction versus temperature for Nd at a typical mass density of $\rho = 10^{-13}$ g/cm³, calculated with the fully relativistic (FR) approach. The black curves and circles refer to Nd I, the red ones to Nd II, the green ones to Nd III, and the blue ones to Nd IV. The solid curves use NIST-corrected ionization energies (Kramida et al. 2015), while the dashed curves use uncorrected values. The circles indicate explicit temperatures at which (NIST-corrected) opacities were calculated for use in the simulation of spectra and light curves.

In addition to calculating FR and SR models, two less-accurate (but faster to compute) FR models were generated in order to test the sensitivity of the macronovae emission to the quality of the atomic data. Configuration interaction (CI) is a method to better describe the correlation between the bound electrons of an atom or ion, and typically results in improved level energies and oscillator strengths (for a more detailed explanation, see, for example, Cowan 1981; Fontes et al. 2015b). The use of CI is crucial for obtaining reasonably accurate atomic structure data for the near-neutral heavy elements considered here. However, due to the smearing of lines caused by the large velocity gradients in the ejecta, it is possible that differing amounts of CI could produce similar spectra, which, if true, would provide more confidence in the fidelity of the simulated spectra, at least from an atomic physics perspective.

In order to test this concept, we generated two additional FR models for Nd: one that includes CI between only those basis states that arise from the same relativistic configuration and one that includes CI between only those basis states that arise from the same non-relativistic configuration. These models are referred to here as “FR-SCR” and “FR-SCNR”, respectively (see Fontes et al. 2015b; Fontes et al. 2016 for additional details). The FR-SCR model is less accurate than the FR-SCNR model, which is less accurate than the FR model described above. All three FR models contain the same number of fine-structure levels, but their energies differ due to the different CI treatments. Additionally, each model contains a different number of lines, as displayed in Table 3. The variant models have fewer lines than the baseline FR model, and those transitions that are common to the three models will typically be described by different oscillator strengths.

Unless otherwise noted, the tables and figures displayed from this point forward refer to the baseline FR model.

3. OPACITIES

TABLE 3
Number of lines per ion stage of neodymium for the FR, FR-SCNR and FR-SCR models (see text).

Ion stage	# of lines		
	FR	FR-SCNR	FR-SCR
Nd I	25,224,451	14,330,369	2,804,438
Nd II	3,958,977	3,222,445	783,275
Nd III	233,822	137,192	51,036
Nd IV	5,784	5,393	2,051

In order to illustrate the basic characteristics of the opacities used in this study, the LTE monochromatic opacity for Nd is displayed in Figure 3 for typical ejecta conditions of $T = 0.5$ eV and $\rho = 10^{-13}$ g/cm³. The left panel displays the complete opacity, with all four contributions (b-b, b-f, f-f and scattering), while the right panel shows the contributions that arise only from free electrons (f-f and scattering) in order to give some indication of the massive differences that occur when the bound electrons are taken into account. The f-f and scattering contributions were obtained from the simple, analytic formulas (Huebner & Barfield 2014) associated with Thomson and Kramers, respectively. The gap between the b-b features and the onset of the b-f edge occurring at ~ 20 eV is due to missing lines that would be present if more excited configurations had been included in the model. Our transport calculations in Section 4 assume this gap is filled in and minimal transport occurs at these energies. We note that a mean charge state of $\bar{Z} = 1.998$ is obtained for these conditions, indicating that the opacity is dominated by Nd III.

In this example, the line-profile function in Equation (1) was chosen to be a standard Voigt profile, which is the convolution of a Lorentz and Gaussian profiles, and takes the natural and thermal Doppler widths as input for a given line. (We note that the latter Doppler broadening is not the same as the previously discussed line-smearing approach, which is addressed below.) The inclusion of the line features dramatically increases the opacity in the optical range (1.65–3.26 eV or 0.751–0.380 μ m) by up to eight orders of magnitude. The absorption in the near-infrared range below 1.65 eV (0.496–1.65 eV or 10.0–0.751 μ m) is also greatly increased, by a few orders of magnitude in this case, indicating that spectra would more likely be observed in the mid-infrared range, at least for these specific conditions.

3.1. Line-smear opacities

As an example of the line-smear opacities used in our light-curve simulations, we present Figure 4. The conditions from Figure 3 ($T = 0.5$ eV and $\rho = 10^{-13}$ g/cm³) are repeated in the right panel, while a lower temperature of $T = 0.3$ eV was chosen for the left panel, which is dominated by contributions from Nd II ($\bar{Z} = 1.000$). In this case, both the black solid curve and the red dashed curve in each panel include b-b features that were calculated with Voigt profiles that included the same set of natural widths, but different Doppler widths. The solid curve represents the traditional thermal broadening evaluated at the LTE temperature, while the dashed curve takes into account the smearing of lines via a much higher effective temperature ($T_{\text{ls}} = 20$ MeV). This temperature is obtained by assuming a velocity gradient of

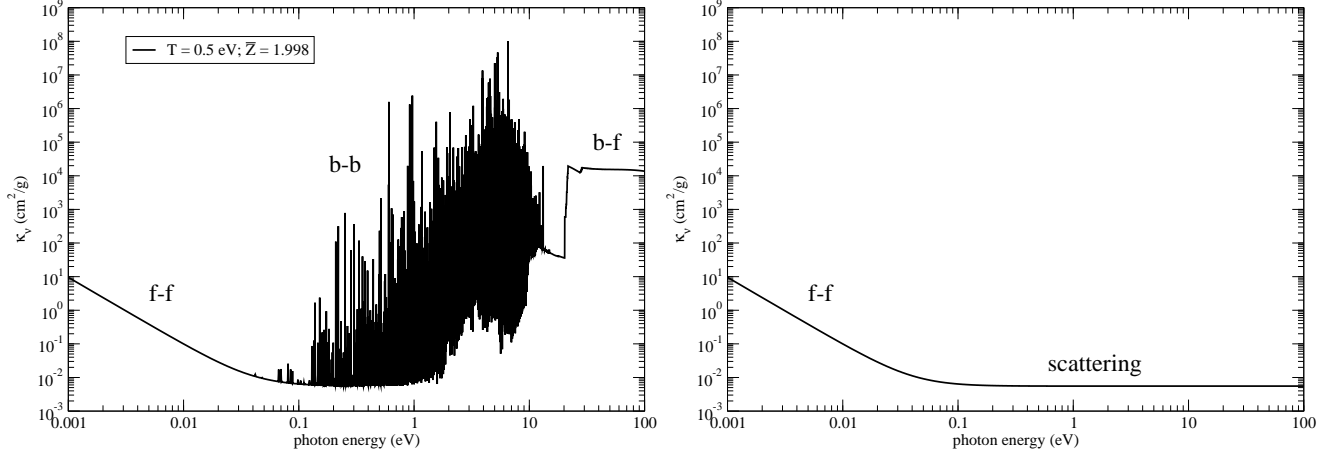


FIG. 3.— The LTE monochromatic opacity for neodymium at $T = 0.5$ eV and $\rho = 10^{-13}$ g/cm³. The left panel displays the complete opacity, which includes the bound-bound, bound-free, free-free and scattering contributions. The right panel displays only the contributions due to free electrons, i.e. the free-free and scattering contributions. The average charge state for these conditions is listed in the legend of the left panel.

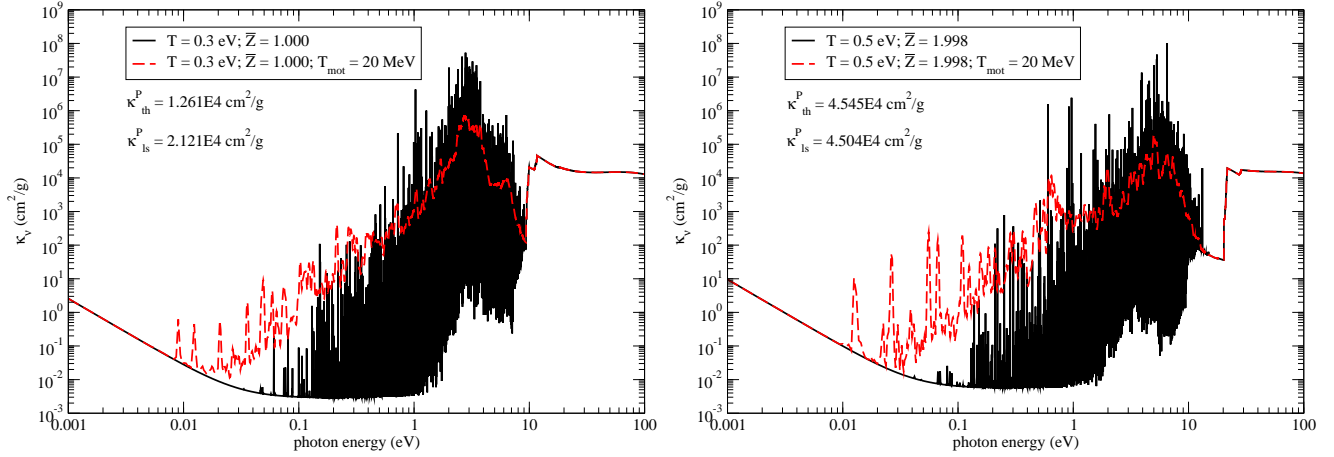


FIG. 4.— The LTE monochromatic opacity for neodymium at $T = 0.3$ eV (left panel) and $T = 0.5$ eV (right panel) for a mass density of $\rho = 10^{-13}$ g/cm³. The solid black curve in each panel includes a bound-bound contribution that was calculated with a Voigt profile using the appropriate natural width and thermal Doppler broadening for each line. The dashed red curve is the same as the black curve, except that the bound-bound contribution was calculated with smeared lines, using an effective Doppler width evaluated at a characteristic temperature of $T_{\text{ls}} = 20$ MeV. The average charge state for these conditions is listed in the legend of each panel. The Planck mean opacities obtained via integration of the thermally broadened and line-smeared opacities are also provided.

$\Delta v/c \sim \Delta \nu/\nu \sim 0.01$, where c is the speed of light. This gradient mimics the velocity gradient across a cell in our 2-dimensional light-curve models and is consistent with our energy group resolution in our transport calculations (see Section 4). We substitute this gradient value into the standard expression for the Doppler width of a transition, i , centered at frequency ν_i , i.e.

$$\Delta \nu_i = \nu_i \left(\frac{2kT}{Mc^2} \right)^{1/2} \quad (2)$$

to obtain an effective temperature, $T = T_{\text{ls}}$, which is used in place of the thermal temperature to smear the lines in the ejecta. In the above expression, $M = A/A_0$ is the mass of an atom of the element of interest, A is the atomic weight and A_0 is Avogadro's number. Using a value of $A = 144$ for Nd, we arrive at an effective temperature $T_{\text{ls}} \sim 20$ MeV. This temperature was used to generate line-smearing opacities for the three lanthanide elements considered here (Ce, Nd, Sm), since they have similar atomic weights, while a temperature of $T_{\text{ls}} = 33$ MeV was chosen for U, based on the linear scaling of the broadening temperature with atomic weight. These effective temperatures were used only in the Doppler-width formula appearing in Equation (2).

From Figure 4, we observe that the effect of the line smearing is to smooth out the jagged b-b features in the opacity, while preserving the area under the curve because the integral of the Voigt profile over all frequencies is normalized to one. Therefore, the line-smearing curves represent a kind of average value of the b-b opacity at each photon energy. This behavior is exhibited between energies of ~ 1 – 10 eV. On the other hand, the area under the curves at lower photon energies is strikingly different, with the line-smearing curve actually exceeding the thermal curve by a significant amount. This difference indicates that the thermal curve contains very narrow lines that are not fully resolved by the chosen grid spacing of photon energies (from Equation (2), the thermal broadening decreases as the photon energy decreases), and so opacity is actually lost in that calculation due to this deficiency. For the curves with line smearing, the lines are sufficiently broad that they are adequately resolved and we obtain a faithful representation of the frequency-dependent opacity within this approximation. So, the use of line smearing in this manner provides the additional (computational) advantage of being able to represent the monochromatic opacities with a reasonable number of photon energy points for the expected range of ejecta conditions, making possible the generation of opacity tables that can be used in an efficient look-up approach in our radiation transport simulations.

The amount of missing opacity that results from the lack of photon-energy resolution can be roughly estimated by comparing the Planck mean opacity, defined as

$$\kappa^{\text{P}} \equiv \int_0^\infty B_\nu(T) \kappa'_\nu d\nu / \int_0^\infty B_\nu(T) d\nu, \quad (3)$$

where $B_\nu(T)$ is the Planck function and κ'_ν indicates that the scattering contribution is omitted from the monochromatic opacity. These mean values are also displayed in Figure 4, indicating a 70% difference at $T = 0.3$ eV, but almost no difference at the higher tem-

perature of $T = 0.5$ eV. The latter null result is partially due to the fact that the peak of the Planck weighting function occurs at a photon energy of $\sim 2.7T$ and the two monochromatic curves agree better at higher photon energies. Despite this similarity in mean values, a significant difference persists in the monochromatic opacities at lower photon energies, as can be seen in the right panel of Figure 4.

A second Nd opacity example is provided in Figure 5, with the conditions ($T = 0.5$ eV, $\rho = 10^{-13}$ g/cm³) being the same as those given in the right panel Figure 4. Monochromatic opacities are presented for the four models described in Section 2: FR, FR-SCNR, FR-SCR, SR. The models produce qualitatively similar results, but there are visible quantitative differences, exemplified by the Planck mean opacities displayed in each panel. The SR model produces the smallest mean value, given by 3730 cm²/g, while the least accurate FR-SCR model has a value of 5309 cm²/g, resulting in a difference of 42%. The most accurate FR model produces an intermediate value of 4504 cm²/g, with the FR-SCNR yielding a similar result. These differences allow us to test the sensitivity of the light curves to changes in the underlying atomic physics that is used to construct the opacity.

As a final illustration, we present in Figure 6 the monochromatic opacities for all four elements in this study at conditions of $T = 0.3$ eV, $\rho = 10^{-13}$ g/cm³. The opacity for each element displays the same basic trends. Each element has $Z \approx 1$ at these conditions due to the similarity in ionization energies, as displayed in Table 2. Therefore, the bound-bound contribution to the opacity is dominated by lines associated with the singly ionized stage. The absorption peaks at a photon energy of ~ 3 eV, with decreasing opacity as the photon energy decreases (or as wavelength increases). However, the detailed line structure is different for each element, with the complexity increasing as the ground configuration of the dominant ion stage moves closer to a half-filled f -shell, for which the complexity of angular momentum coupling is maximal. In all cases, a significant amount of opacity is missing at lower wavelengths when thermally broadened lines (black, solid curves) are used, but is captured when smeared lines are considered (red, dashed curves).

3.2. Justification for line-smearing opacities

The issue of which method to choose for calculating opacities in a moving medium is not straightforward. For circumstances with a lack of strong line overlap and insignificant fluorescence, the Sobolev approach is well founded. However, the justification for reducing the optical depth under the Sobolev approximation is less obvious if a photon absorbed by a line resonance often leaves with a significantly different energy, i.e. fluorescence. This issue is similar to the discussion of whether to use Rosseland or Planck opacities for a given problem, e.g. (Pomraning 1971). Typically, it is assumed that if one is focused on the line opacities (e.g. line emission), the Planck opacity is better. However, if one is focused on radiative heat transfer, the opacity between the lines where radiation can flow more freely is most important. As such, most calculations that focus on heat flow use the Rosseland opacity, e.g. (Ganapol & Pomraning

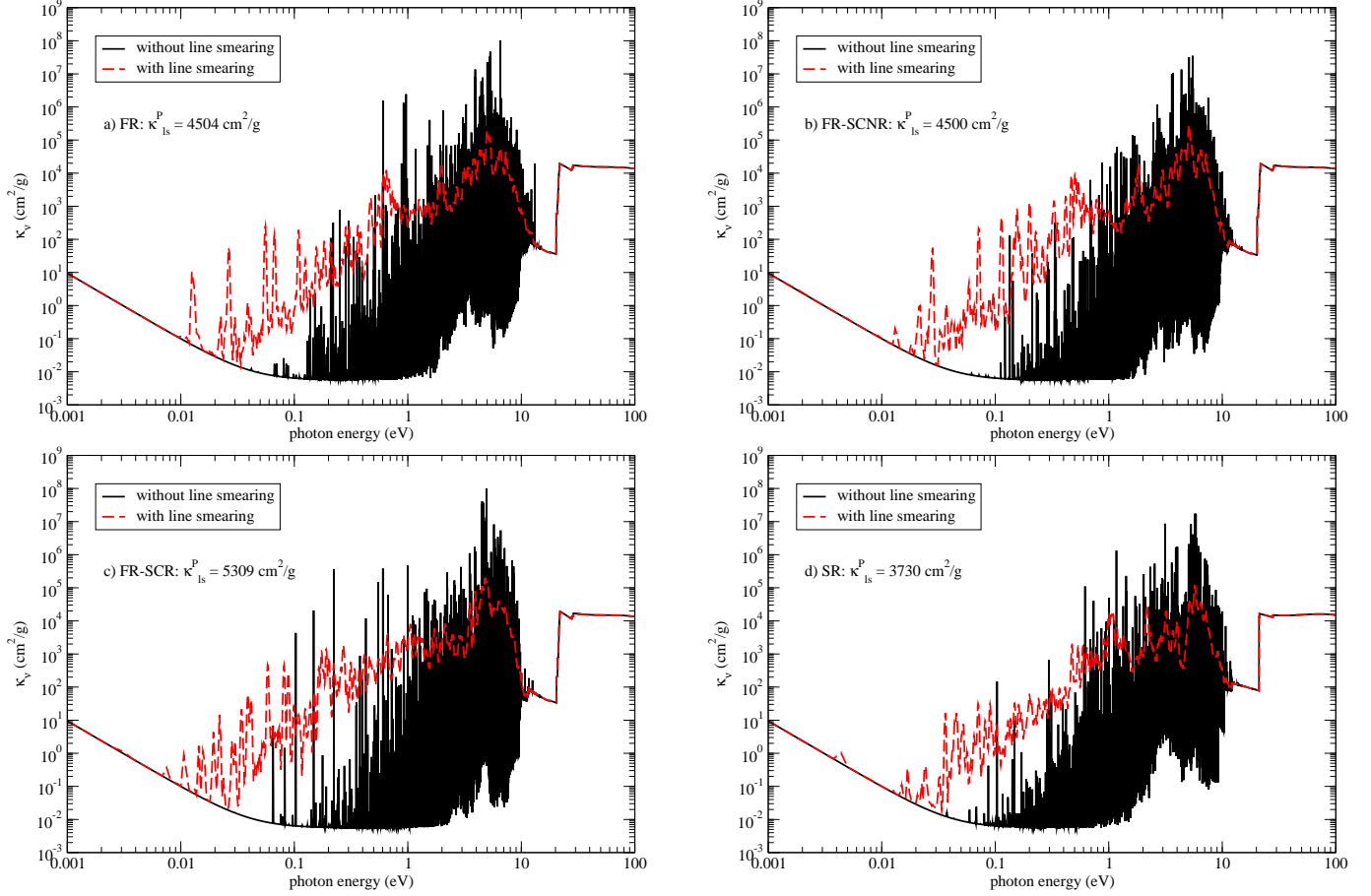


FIG. 5.— The LTE monochromatic opacity for neodymium at $T = 0.5$ eV and $\rho = 10^{-13}$ g/cm³ using four different models described in the text: a) FR, b) FR-SCNR, c) FR-SCR, and d) SR. The solid black curve in each panel includes a bound-bound contribution that was calculated with a Voigt profile using the appropriate natural width and thermal Doppler broadening for each line. The dashed red curve is the same as the black curve, except that the bound-bound contribution was calculated with smeared lines, using an effective Doppler width evaluated at a characteristic temperature of $T_{\text{is}} = 20$ MeV. The Planck mean opacity obtained via integration of the line-smeared opacity is also listed in each panel.

1987). Similarly, the expansion-opacity formulation is an approximation for estimating the opacity through a medium with a velocity gradient (Karp et al. 1977). This method uses the Sobolev line-strength approximation (Sobolev 1960) for radiation flow through velocity gradients. Type Ia supernovae modeled with this expansion opacity can reproduce bolometric light curves, but the resulting spectra are too blue (Pinto & Eastman 2000). To address this discrepancy, Pinto & Eastman (2000) argued that a correction factor was needed to include fluorescence in the lines, neglected in the Sobolev approximation (Sobolev 1960). The correction factor is chosen to match the Type Ia light curves.

The case has been made for relatively high fluorescence in Type Ia supernovae by Pinto & Eastman (2000) and by Kasen et al. (2006). A similar effect has been suggested by Kasen et al. (2013) for NS ejecta. As previously mentioned, the lanthanides and actinides are expected to provide the dominant contribution to the ejecta opacity. The complex energy-level structure of these elements supports the possibility of high fluorescence. As an illustrative example, we consider Figure 7, which displays the radiative-decay branching ratios for transitions of various strengths in Nd II. The branching ratio for radiative decay from an upper level u to a lower level l

is given by the standard expression

$$B_{ul} = \frac{A_{ul}}{\sum_k A_{uk}}, \quad (4)$$

where A_{ul} is the Einstein coefficient for spontaneous radiative decay from level u to l . The summation in the denominator includes all allowed decay channels from the upper level u . The two panels in Figure 7 display the branching ratio in color-contour format, with the intensity representing the probability that a photon absorbed with a particular energy given on the x axis will be re-emitted at an energy given on the y axis (assuming no other processes, such as electron collisions, play a role in destroying the upper level u). The left panel displays the branching ratio for the strongest set of absorption lines in our model for Nd II, i.e. $f_{lu} > 0.1$, where f_{lu} is the absorption oscillator strength for a photon absorption from level l to level u . (Here, we employ the dual-index form of the oscillator strength, rather than the single-index form displayed in Equation (1).) The right panel displays the branching ratio for a weaker set of Nd II lines in the adjacent range given by $0.01 < f_{lu} \leq 0.1$. The color contours were obtained by averaging the pointwise B_{ul} values over logarithmically spaced bins in the x and y directions. Branching ratios that appear on the $x = y$

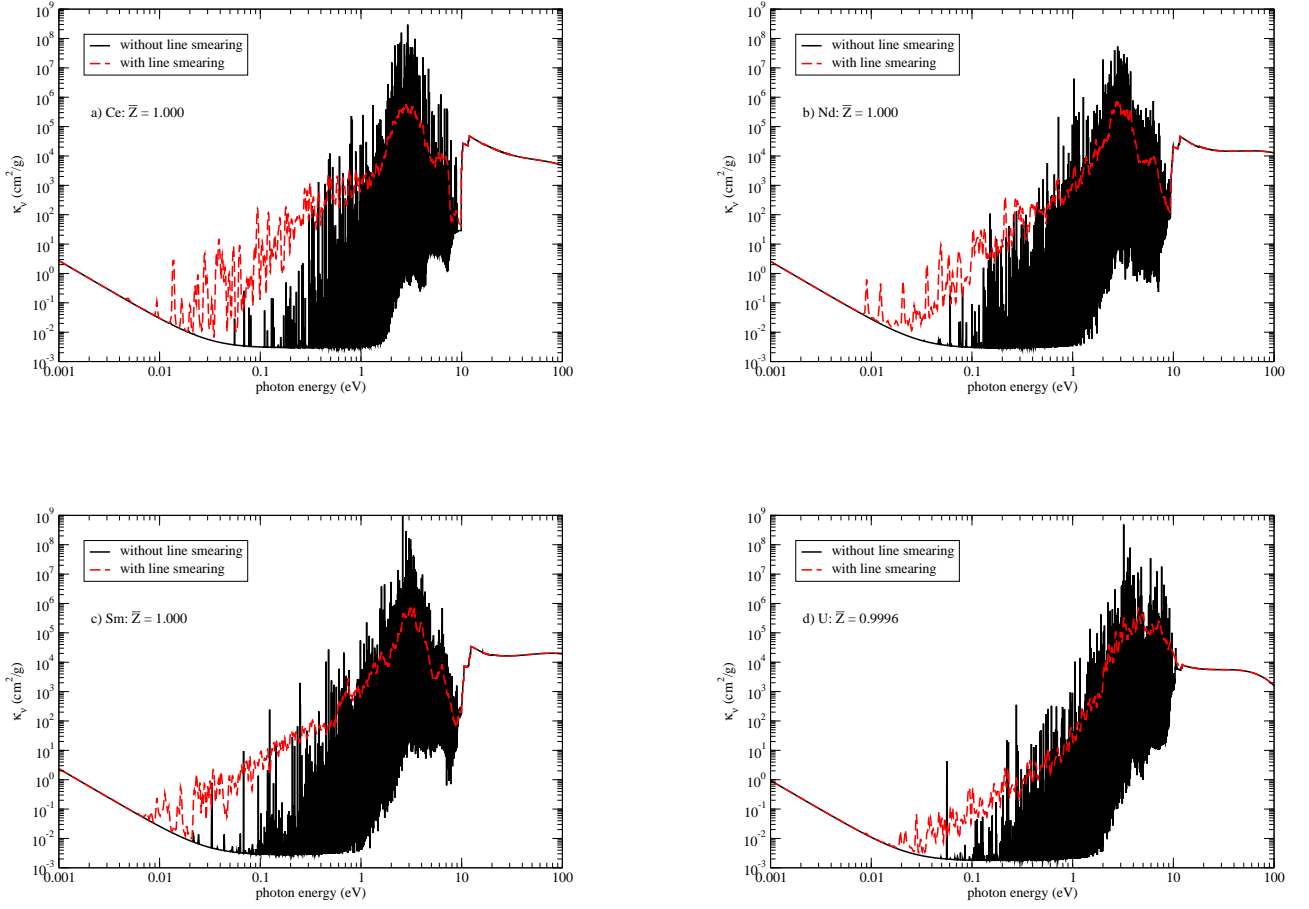


FIG. 6.— The LTE monochromatic opacity for the four elements considered in this work at $T = 0.3$ eV and $\rho = 10^{-13}$ g/cm³: a) cerium, b) neodymium, c) samarium, and d) uranium. The solid black curve in each panel includes a bound-bound contribution that was calculated with a Voigt profile using the appropriate natural width and thermal Doppler broadening for each line. The dashed red curve is the same as the black curve, except that the bound-bound contribution was calculated with smeared lines, using an effective Doppler width evaluated at a characteristic temperature of $T_{\text{ls}} = 20$ MeV for the three lanthanides and $T_{\text{ls}} = 33$ MeV for uranium. The mean charge is also displayed in each panel.

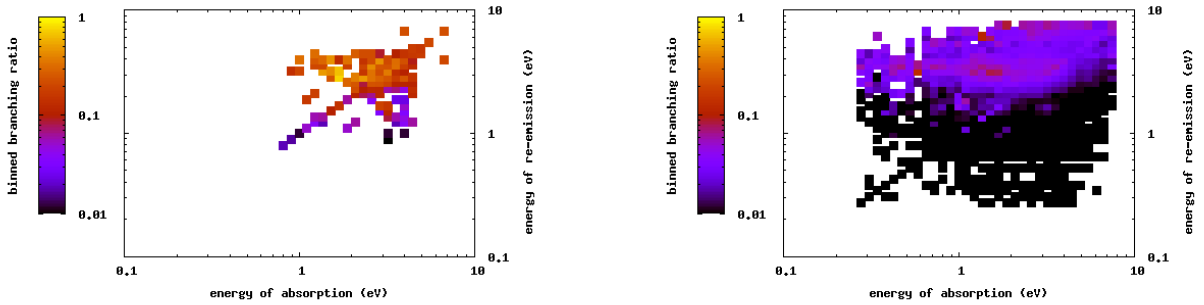


FIG. 7.— Radiative-decay branching ratios for transitions of various strengths in Nd II. The left panel displays branching ratios for the strongest set of absorption lines with oscillator strengths that satisfy $f_{lu} > 0.1$. The right panel displays branching ratios for a weaker set of absorption lines with oscillator strengths in the range $0.01 < f_{lu} \leq 0.1$.

diagonal line correspond to scattering, i.e. re-emission at the same energy possessed by the absorbed photon, while the off-diagonal values represent fluorescence.

The strongest set of lines considered in the left panel displays a mixture of both fluorescence and scattering. These lines typically appear as strong absorption features at optical and higher photon energies, where the monochromatic opacity peaks for representative macronova conditions, such as those considered in Figures 3–6. The weaker set of lines considered in the right panel displays a significant amount of fluorescence, with the re-emitted energy spread across a much broader range. There are significantly more options for absorption and re-emission in this set due to photo-absorption from the numerous excited levels that lie above the ground (and lowest-lying excited) levels, as well as due to the quantum selection rules that determine which transitions are allowed. From this type of study, we find that strong fluorescence, spread over a broad range of re-emission channels, persists for progressively weaker absorption lines. A subset of these weaker, fluorescing lines permit radiation to escape the ejecta, which produces the light curve.

Of course, the situation is more complicated than indicated by the above illustrative example. A more thorough study should take into account the actual population of the lower level for each transition (see the factor of N_i in Equation (1)) at a given temperature and density. Furthermore, collisional destruction of the upper level, u , may be pertinent. Such issues have been studied, for example, in the context of the expansion-opacity formalism for Type Ia supernovae by Pinto & Eastman (2000) in their Figure 4, which displays the cascade matrix for a particular set of conditions. Nevertheless, our branching-ratio example suggests that fluorescence is of primary importance in the lanthanide (and actinide) contribution to the ejecta opacity.

We explore the consequences of the assumption of strong fluorescence for macronovae in the present work using our line-smeared approach. Our method represents an alternative transport approximation that puts a primary emphasis on the fluorescence phenomena compared to an expansion opacity with a calibrated correction factor. For Type Ia spectra, the higher opacity in the line-smeared type of calculation moves the photosphere outward and the lower effective temperature produces a better match with observation compared to the expanding-photosphere method if the fluorescence correction is omitted in the latter case. Similarly, our approach produces significant differences in the macronova light curves compared to those produced via the opacity-expansion formalism. The expanding-photosphere versus the full-line opacity methods represent two possible options for calculating the supernova opacity, but, just like the Rosseland and Planck mean opacities, these methods are approximations. Because of the importance of fluorescence, we believe the method employed here is more appropriate for supernova and macronova light-curve calculations.

In support of our approach, we demonstrate the effectiveness of our line-smeared opacities in modeling a simplified W7 problem for a pure-Fe outflow, but with the same radioactive heating as in the standard W7 case. This example uses the **SuperNu** radiation transport code,

which has been previously shown to produce light curves that are in good agreement with those generated with the PHOENIX code (Wollaeger & van Rossum 2014) for the W7 Type Ia light-curve problem, as well as an observation of an abnormal Ia supernova (van Rossum et al. 2016). (The discrepancy in peak luminosity described in Wollaeger & van Rossum (2014) was reported to be 10–15%, but has subsequently been reduced to 5–10%, due to differences in gamma-ray energetics (van Rossum & Wollaeger, unpublished).) Those **SuperNu** W7 calculations employed a Kurucz line list that was “regrouped” for computational efficiency. This regrouping is similar to our line-smeared approach, i.e. individual lines are combined in such a way that the resulting opacity has the same area under the curve as the ungrouped opacity. As mentioned previously, an advantage of this type of approach over the Sobolev line-expansion method is that it does not require a fluorescence correction to obtain physically reasonable light curves.

In Figure 8, we compare the total luminosity and UB-VRI AB magnitudes for the W7 problem obtained with opacities from the Kurucz line list and from our line-smeared approach. The agreement is quite good for the total luminosity, within $\sim 20\%$ near and after peak luminosity. The broadband light curves indicate that the bulk emission is in a similar location in frequency around peak bolometric luminosity. The biggest discrepancy occurs in the I band due to the dip in the tabular result. At the time of peak total luminosity, the differences in the broadband luminosities (converting from magnitude to equivalent luminosity) are: $\sim 18\%$ in the U band, $\sim 15\%$ in the B band, $\sim 7\%$ in the V band, $\sim 15\%$ in the R band and $\sim 90\%$ in the I band (due to the dip).

Next, we present a sample comparison of single-element opacities generated with the expansion-opacity and line-smeared methods for typical macronova conditions. As mentioned previously, the expansion-opacity method (Sobolev 1960; Castor 1974; Karp et al. 1977) employed by Kasen et al. (2013); Barnes & Kasen (2013) to simulate NSM light curves applies to the bound-bound contribution to the opacity and involves a discrete sum over all lines. The approach relies on the assumption of a homologous expansion and is characterized by an expansion time, t_{exp} . The relevant wavelength range is divided into bins denoted by index j , $\Delta\lambda_j$, and all lines within a bin are summed to obtain the opacity for that range. The expression for the opacity associated with bin j is given by

$$\kappa_{\text{exp}}^{\text{b-b}}(\lambda_j) = \frac{1}{\rho c t_{\text{exp}}} \sum_i \frac{\lambda_i}{\Delta\lambda_j} (1 - e^{-\tau_i}), \quad (5)$$

where t_{exp} is the time since mass ejection, the summation index i extends over all possible bound-bound transitions, λ_i is the associated rest wavelength, and τ_i is the corresponding Sobolev optical depth, i.e.

$$\tau_i = \frac{\pi e^2}{m_e c} N_i |f_i| t_{\text{exp}} \lambda_i. \quad (6)$$

In Figure 9, we present the monochromatic opacity of Nd at $T = 4,000$ K (0.345 eV) and $\rho = 10^{-13}$ g/cm³, generated with the FR model. There are two curves, one representing the bound-bound contribution obtained from the current line-smeared approach, Equation (1),

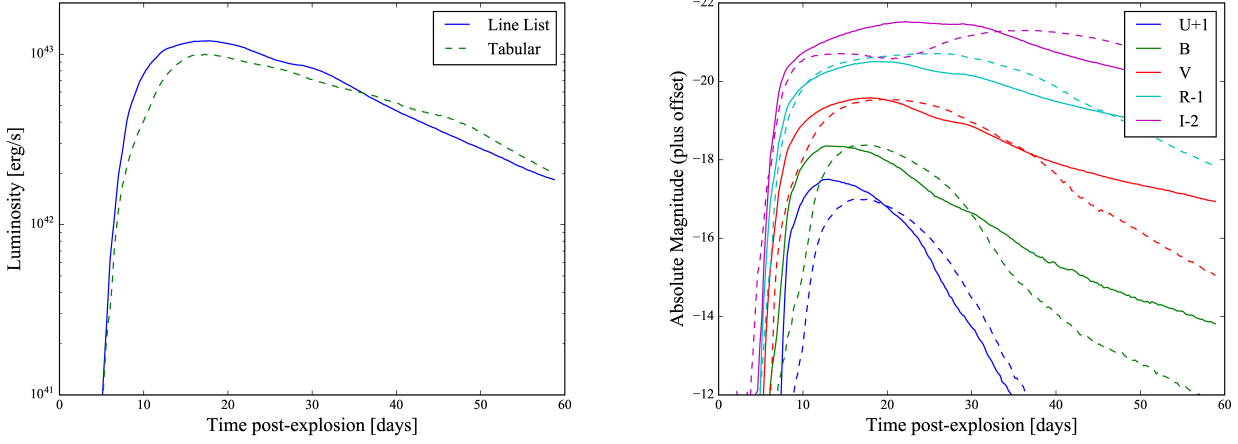


FIG. 8.— Left panel: the total W7 luminosity calculated with *SuperNu* using opacities obtained from the Kurucz line list (solid, blue curve) and from our tabular, line-smeared approach (dashed, green curve). Right panel: absolute magnitude versus time since explosion for the U, B, V, R and I bands. The solid curves represent the line-list opacities and the dashed curves represent the present line-smeared opacities. For clarity, the U-, R- and I-band curves have been shifted by +1, -1 and -2, respectively.

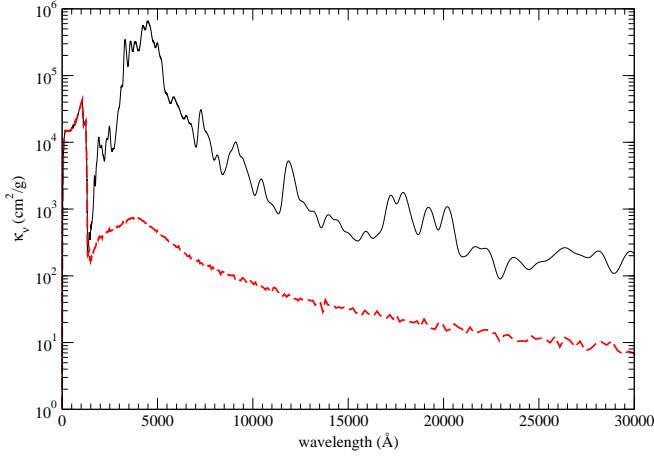


FIG. 9.— The LTE monochromatic opacity for neodymium at $T = 4,000$ K (0.345 eV) and $\rho = 10^{-13}$ g/cm³ using the line-smeared (black solid curve) and Sobolev expansion (red dashed curve) methods. The expansion opacity was calculated at a time since ejection of $t_{\text{exp}} = 1$ day and wavelength binning of $\Delta\lambda = 0.01\lambda$. The line-smeared method produces opacities that are typically one to two orders of magnitude higher than the expansion opacity.

and the other from the expansion-opacity method, Equation (5). (For completeness, we mention that the two corresponding curves generated with the SR model (not shown) are quantitatively similar to the two FR curves displayed in this figure.) The opacity is plotted versus wavelength instead of energy, and the conditions were chosen in order to facilitate direct comparison with Figure 8 of Kasen et al. (2013). The line-smeared approach produces an opacity that is one or more orders of magnitude greater than the expansion method over much of the wavelength range. As a consequence, the luminosity will be significantly diminished when line-smeared opacities are used to simulate light curves, compared to expansion values.

We note that the expansion opacity in Figure 9 is qualitatively similar to that displayed in Figure 8 of Kasen et al. (2013), with the peak value of the b-b contribution occurring at $\sim 5,000$ Å and monotonically decreasing at higher wavelengths. However, the peak value

is about three times larger in the present case, providing a rough measure of the uncertainty in current opacity calculations as they pertain to macronova conditions. This discrepancy is somewhat surprising due to the fact that the same list of configurations, resulting in the same number of lines (see the Nd data listed in Table 1), was used in both cases. The differences are perhaps an indication of how difficult it is to perform accurate atomic structure calculations for such complicated atoms and ions. Qualitative differences occur at the higher wavelengths, where the present curve is significantly smoother and passes through the relatively large peak-to-valley variations displayed by the curve of Kasen et al. (2013). We were able to obtain such large oscillations in our calculations by employing a linearly spaced wavelength grid, rather than the logarithmically spaced grid obtained from the prescription $\Delta\lambda = 0.01\lambda$.

3.3. Opacity tables

In order to perform radiation-transport calculations in an efficient manner, opacity tables were generated for the four elements of interest using prescribed temperature and density grids that span the range of conditions of interest. The temperature grid consists of 27 values (in eV): 0.01, 0.07, 0.1, 0.14, 0.17, 0.2, 0.22, 0.24, 0.27, 0.3, 0.34, 0.4, 0.5, 0.6, 0.7, 0.8, 0.9, 1.0, 1.2, 1.5, 2.0, 2.5, 3.0, 3.5, 4.0, 4.5, and 5.0. Specific temperature values are also indicated by circles in the ionization balance plot of Figure 2. The density grid contains 17 values ranging from 10^{-20} to 10^{-4} g/cm³, with one value per decade.

4. SIMULATED LIGHT CURVES

To provide a first look at how these different opacities affect the macronova emission, we simulate a series of spectra and light curves for our different opacities. We use a simplified ray-trace transport code to calculate the macronova light curves for different opacities and atomic physics models, different merger models, and different viewing angles.

We consider three merger models from Rosswog et al. (2014) and Grossman et al. (2014) with the following binary masses (see Table 4): $1.4 + 1.4 M_{\odot}$, $1.8 + 1.2 M_{\odot}$

and $1.6 + 1.2 M_{\odot}$ 18–25 ms after the onset of the merger process. For these three models, we consider only tidal ejecta material with velocities above the escape velocity. The ejecta masses are 0.022, 0.043 and $0.041 M_{\odot}$, and the energies are 1×10^{50} erg, 3.6×10^{50} erg and 2×10^{50} erg for, respectively, the $1.4 + 1.4 M_{\odot}$, $1.6 + 1.2 M_{\odot}$ and $1.8 + 1.2 M_{\odot}$ models. We stress that these are just one set of merger models, and the assessment of exact ejecta properties from different mergers is still an area of active research. In each model, the particles in the smooth particle hydrodynamics calculations carried information of the particle positions at the end of the calculation as well as the masses and velocities of the ejecta. Assuming the ejecta are ballistic at the end of the calculations (Rosswog et al. (2014) demonstrated the homologous expansion of this ejecta), we can use this particle information to calculate the 3-dimensional distribution of matter.

TABLE 4
PROPERTIES OF OUR MERGER MODELS.

Masses (M_{\odot})	M_{ejecta} (M_{\odot})	Energy _{ejecta} (10^{50} erg)
1.4+1.4	0.022	1.0
1.6+1.2	0.043	3.6
1.8+1.2	0.041	2.0

We assume the energy deposition from the decay of radioactive material given by Metzger et al. (2010), which decays with time ($t^{-\alpha}$ with $\alpha \approx 1.3$). As in many of the light-curve calculations of Type Ia supernovae, we assume this energy deposition dominates the temperature structure of the ejecta (with homologous outflows into the low-density media expected in neutron star mergers, shocks are not important).

The temperature profile is calculated using the energy from the radioactive decay. We include a simplified 1-temperature diffusion approximation to incorporate the radiation energy transport within our coarse transport grid. This 1-T diffusion scheme has been compared to analytic prescriptions for light curves of Type Ia supernovae (Arnett et al. 2016) and pair-instability supernovae (de la Rosa 2017, in preparation). With the temperature profiles set by this energy, we calculate the macronova spectra and luminosities via ray-trace post-process on the opacities. We linearly interpolate our opacity database over density and temperature to estimate the opacity for each transport zone. For the coarse resolution in our 2-dimensional simulations, the velocity change across a zone is $\Delta v/c \sim 0.005$ – 0.01 , which corresponds to a comparable frequency resolution due to the homologous nature of the flow. For each zone, we shift the energy of our radiation for each ray-trace photon energy to the rest frame at zone center of the ejecta and obtain an opacity from our tables. As the photons traverse the zone, they are alternatively bluer/redder than this zone center. This method would allow us to reproduce P-Cygni profiles, but because there are many strong lines in any energy bin, such profiles are not resolved. As such, the opacity tables described in Section 3.3 were averaged over frequency such that $\Delta\nu/\nu$ was around 1%. This procedure resulted in a number of frequency groups ranging from 150–1500, logarithmically spaced between 40 – 10^7 Å, depending the temperature.

Averaging within these larger groups was accomplished by taking an energy-weighted sum of the monochromatic opacities that are present in the more spectrally resolved tables. This approach allows us to conduct a wide parameter study while including a fairly detailed group structure for the atomic physics. For simplicity, we have assumed that the ejecta is cylindrically symmetric, comparing the luminosities in only two directions, on axis and in the radial direction.

Note that this light-curve scheme is approximate, and these results are focused more on providing qualitative features of these new opacities. In an upcoming paper (Wollaeger et al., in preparation), we present detailed multi-dimensional, time-dependent Monte Carlo calculations of the macronova emission.

4.1. Comparing Spectra

As indicated above, the approximations made in the atomic physics and how we implement them can drastically alter the opacity, i.e., the Sobolev approximation produces an opacity that, over a wide range of wavelengths, is more than an order of magnitude lower than that predicted by an approach that smears each line while preserving the overall opacity. With our transport simulations, we can calculate how these opacities, and their implementation, affect the emission predictions from macronovae.

First, we note that, even though a minimal amount of smearing will merge many lines in our opacity calculations, any individual element will have gaps in its opacity. Figure 10 shows the spectra produced if we assume the opacity is dominated by a single element, with four curves representing Nd, Ce, Sm, and U. (The significant UV emission that occurs for Ce between ~ 7 – 10 Å is an artifact resulting from the gap between the bound-bound lines and bound-free edge mentioned previously in Section 3.) For any individual element, gaps exist that allow flux out of the merged system. However, when a mixed material, obtained by combining a broad range of elements, is considered, such gaps will be filled and the luminosity will be pushed toward longer wavelengths. As an illustration of this effect, see the black curves in Figure 10, which represent a mixed material with combined opacity consisting of 30% each of Nd, Sm, and Ce, plus 10% U, representative of the third r -process peak. In most NSM models, roughly half of the material consists of lighter elements with much lower opacities, especially in the near infra-red (nIR). By assuming the stated composition, we overestimate the effect of lanthanides. We have modeled an additional test case in which the opacity was halved, assuming the lighter elements make up half of the atoms and do not contribute to the opacity. In this model, the optical contribution can be 2 orders of magnitude brighter in the first 8 hours (although the luminosity is still dominated by nIR and IR), but it drops significantly after that, again not contributing to the light curve. The nIR contribution is brighter in this scenario, but still an order of magnitude dimmer than the IR at peak. This behavior is studied in more detail in Wollaeger et al. (in preparation).

At 10 d, the luminosity is miniscule at short wavelengths, rising only for photons with wavelengths above $10,000$ Å. Whether the luminosity exceeds some nom-

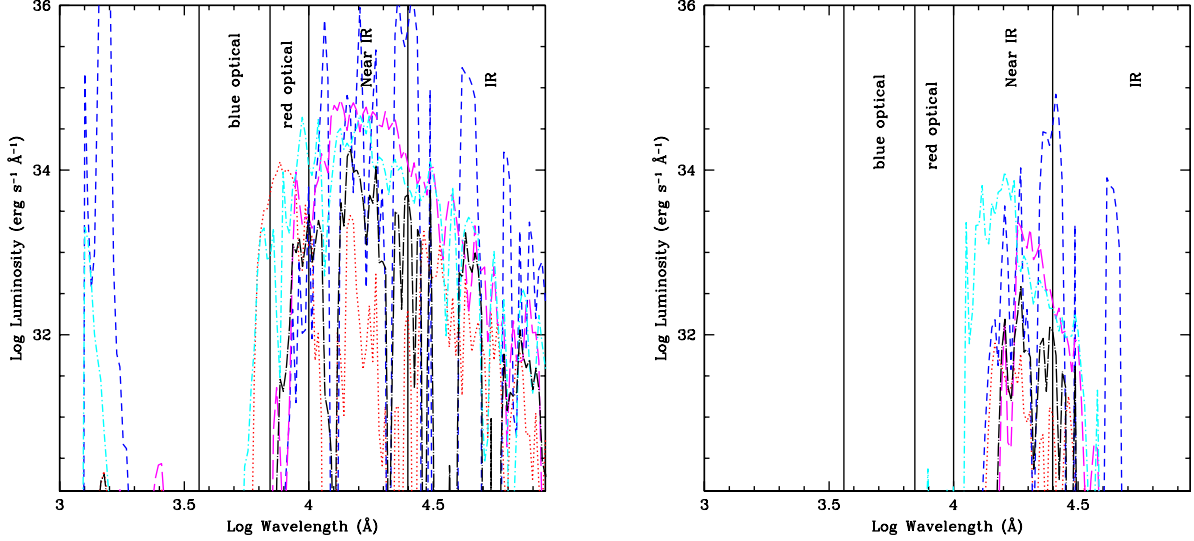


FIG. 10.— Luminosity versus wavelength, assuming single-element species, for a merger system consisting of two $1.4 M_{\odot}$ neutron stars at 1 d (a) and 10 d (b). For these studies, we consider Nd (red), Ce (blue), Sm (cyan) and U (magenta) using the semi-relativistic opacities. The black curve is produced by combining these elements to form a single opacity (see text for details). Gaps in the opacity allow higher luminosities at some wavelengths, but combining them fills in these windows, reducing the luminosities in these wavelength bands.

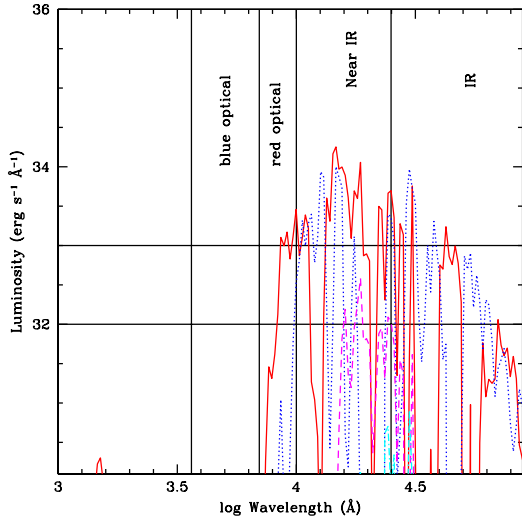


FIG. 11.— Luminosity versus wavelength for our $1.4 + 1.4 M_{\odot}$ merger model at 1 and 10 d for the semi-relativistic (solid/dashed) and the fully relativistic (dotted/dot-dashed) opacities. The red (solid) and magenta (dashed) curves represent the semi-relativistic model at 1 and 10 d, respectively. The blue (dotted) and cyan (dot-dashed) curves represent the fully relativistic model at 1 and 10 d, respectively. The observed spectrum corresponds to what lies above some detection limit. The horizontal lines depict two different detection limits (10^{32} , 10^{33} $\text{erg s}^{-1} \text{\AA}^{-1}$), respectively.

inally measurable value (say, $10^{32} \text{ erg s}^{-1} \text{\AA}^{-1}$ at 5 d) above a wavelength of 11,000 \AA or 15,000 \AA depends upon which element we choose. At 5 d, the luminosity is above this value for the combined semi-relativistic opacity only for photons above 15,000 \AA . These differences define the exact bands in the infra-red that dominate the opacities.

We can use these combined opacities to study the importance of our different atomic physics models. For example, Figure 11 compares the spectra obtained from the combined opacities for the semi-relativistic and fully

relativistic models. At 2 d, the luminosity exceeds $10^{32} \text{ erg s}^{-1} \text{\AA}^{-1}$ for wavelengths above 13,000 \AA for the semi-relativistic opacity, compared to 12,000 \AA for the fully relativistic opacity. This difference in wavelength is, by far, the largest effect on the spectra due to the various models considered here. In contrast, the use of opacities from the most-approximate FR-SCR model produces shifts of less than a few thousand \AA compared to the FR model.

Aside from the shift toward mid-infra-red bands, there are no clear spectral lines from these lanthanide opacities, and it may be difficult to identify macronovae from their spectra.

4.2. Light Curves

These shifts in the light curves produce trends in the broad-band luminosities. For these light curves, we consider the luminosities in four broad bands: the infra-red (we define “IR” as photons with energies between 0.124–0.496 eV or 10.0–2.5 μm), near infra-red (“nIR” is defined as photons between 0.496–1.24 eV or 2.5–1 μm), red-band optical (defined as photons between 1.24–1.77 eV or 1–0.7 μm), and blue-band optical (defined as photons between 1.77–3.44 eV or 0.7–0.36 μm).

Figure 12 shows the IR, nIR and red-band optical light curves for our three models using both our relativistic and semi-relativistic approximations. For our models, the optical band is only bright when the radiation first emerges, limited to a very short-duration, low energy burst of photons. Such results are sensitive to the transport calculation and we defer their discussion to a later study. Most of the radiation is emitted in the infra-red energy range, with a lower flux in the nIR. Our ejecta masses vary by a factor of two, and the resultant luminosities vary by roughly a factor of 3. Without a broader range of ejecta masses, we can not firmly determine the importance of the ejecta mass, but we are consistent with the roughly linear dependence on this mass determined

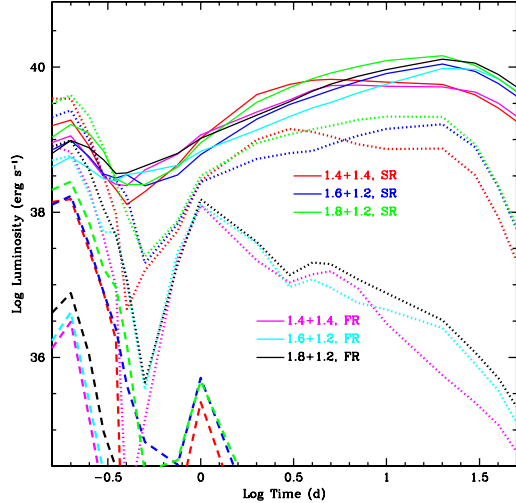


FIG. 12.— IR (solid), nIR (dotted) and red-band optical (dashed) luminosities versus time for our three merger models using both the fully relativistic and semi-relativistic opacities. We do not show the blue-band optical as it appears only at early times when the ejecta first becomes optically thin (the equivalent of shock “breakout”, although this is closer to shock emergence). This emergence emission will be sensitive to the details of the transport calculations and we defer this calculation to a more focused study on that particular physics.

by Barnes & Kasen (2013).

The blue-band optical emission is extremely low, never peaking above $10^{35} \text{ erg s}^{-1}$ and dropping below $10^{30} \text{ erg s}^{-1}$ within a fraction of a day. The red-band optical is brighter, peaking above $10^{38} \text{ erg s}^{-1}$, but also dropping within a fraction of a day. The nIR band is most sensitive to the opacities, where the fully relativistic opacities cause the emission to decrease sharply after the first day, falling below $10^{37} \text{ erg s}^{-1}$ after about 8 d. This behavior is a consequence of a slight shift in the FR versus SR spectrum; compare the red (solid) and blue (dotted) curves in Figure 11 at x-axis values of 3.7–3.8 Å. With the semi-relativistic opacities, this light curve remains bright (above $10^{39} \text{ erg s}^{-1}$ for 10 d). The IR light curve is much broader and peaks above $10^{40} \text{ erg s}^{-1}$. Understanding these opacities is critical in determining the detectors needed to observe these mergers.

The bulk of our luminosity is emitted in the IR and we can compare this luminosity to the bolometric light curves from past work. Figure 2 in Barnes & Kasen (2013) shows the bolometric light curves for a range of simplified models with ejecta masses ranging from 0.001 – $0.1 M_{\odot}$. In that work, the characteristic velocity is parametrized as a fraction of the speed of light, ranging from 0.1 – 0.3 times the speed of light. Our models are in the massive range of their suite (0.02 – $0.043 M_{\odot}$) with characteristic velocities below 0.1 times the speed of light. As such, we expect our light curves to be broader than most of Barnes & Kasen (2013). In addition, as we have discussed, our opacities are more than an order of magnitude higher than those of Barnes & Kasen (2013), further broadening our light curves and producing peak fluxes that are roughly an order of magnitude lower. This order of magnitude decrease in the flux demonstrates the sensitivity of the predicted light curves to the manner in which the opacities are calculated.

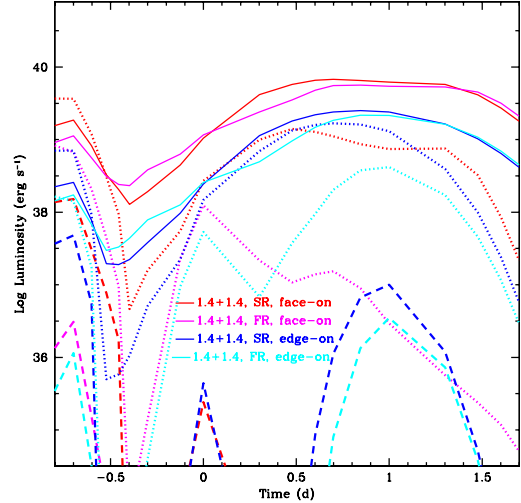


FIG. 13.— IR (solid), nIR (dotted) and red-band optical (dashed) luminosities versus time for our $1.4+1.4 M_{\odot}$ merger using both the fully relativistic and semi-relativistic opacities.

Figure 13 shows the variation in the macronova light curves, comparing the face- and edge-on luminosities of a binary NS system composed of two $1.4 M_{\odot}$ components. Typically, the edge on luminosities are 3–4 times lower. The sensitivity of the light curves to shifts in the spectra do allow larger differences in the nIR, where the nIR emission from an edge-on burst is over an order of magnitude brighter than that of its semi-relativistic counterpart.

4.3. Caveats

With our SR opacities more than 10–100 times greater in the optical and near-IR than any current calculation, it is not surprising that our emission is dimmer than past work. The comparisons are even more extreme for our FR opacities, but bear in mind that these light-curve calculations are designed to demonstrate the variations caused by the uncertainties in the opacities, and may not be the final macronova light curves. A number of uncertainties in the light-curve models may yet change the final theoretical light curves.

Although our ray-tracing transport is not as sensitive to the low spatial resolution of typical multi-dimensional light-curve calculations, our simplified transport scheme does not follow the true temperature evolution of the ejecta. As the material becomes more transparent to gamma-rays and, ultimately, electrons emitted during the decay of our r -process elements, the energy deposition will decrease (Hotokezaka et al. 2016; Barnes et al. 2016). We do not include this effect and our light curves are almost certainly broader than that produced by full transport calculations. As we understand these uncertainties more fully, we expect shifts in these light curves. To test the importance of this effect at late times, we compare our standard model with one that assumes the energy deposition decreases dramatically after 10 d assuming a larger fraction of the gamma-rays and energetic electrons escape (see Figure 14). Although artificial, this figure provides an idea of the importance of accurate decay models.

Additional uncertainties include our initial conditions.

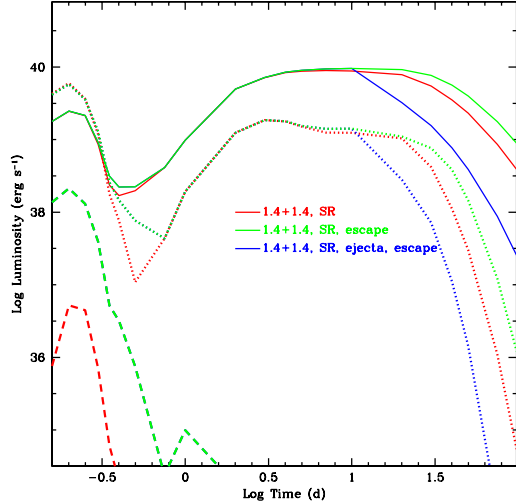


FIG. 14.— Luminosity versus time for three variations on the $1.4+1.4M_{\odot}$ models. Comparisons for IR (solid), nIR (dotted) and red-band optical (dashed) are made between our standard model (red) and two variations that explore the impact of uncertainties discussed in Section 4.3. These include a model where gamma-ray deposition is reduced by a factor that varies exponentially in time after 10 d (green), and a model that includes this reduced-gamma deposition, as well as an increase in the mass of the tidal ejecta (blue). The increased mass comes from including material in the tidal ejecta if it has a velocity greater than one half of the escape velocity, rather than just the escape velocity.

For example, the amount of ejecta depends both on the exact simulation and on the time at which we use these simulation results. In our models, we used the “ejecta” produced in the first 18–25 ms of a merger simulation. Had we used later-time models, some of the “bound” material could gain energy to become unbound. To test this hypothesis, we performed a simulation where the tidal ejecta includes any material with velocities exceeding half the escape velocity (instead of our standard full escape velocity). We assumed that this material does not decelerate beyond this ejection velocity and recalculated the light curve. Figure 14 shows the revised light curve from these increased ejecta runs. The corresponding magnitude plot (assuming the AB magnitude in a band is set to $-2.5 \log_{10}(\text{Luminosity}/(4\pi d^2)) - 48.6$ where $d = 200 \text{ Mpc}$) is shown in Figure 15. AB magnitudes, instead of erg s^{-1} , were chosen for this figure as a convenience to observers.

Finally, we have assumed that the ejecta are dominated by the r -process ejecta in the tidal tails. Winds and shocked ejecta from the newly-formed proto-neutron star (as well as the torus of high angular-momentum material around this core) can produce more elements near the iron peak, and these elements have lower opacities, particularly in the nIR energy bands. For cases where considerable mass is ejected through winds and shocks, the light curves could be much brighter.

5. SUMMARY

The ejecta from the merger of two neutron stars have the potential to produce an EM signal that can be used, in conjunction with a GW detection, to both pinpoint the GW source and better understand the physics of these mergers. However, past calculations of the emission

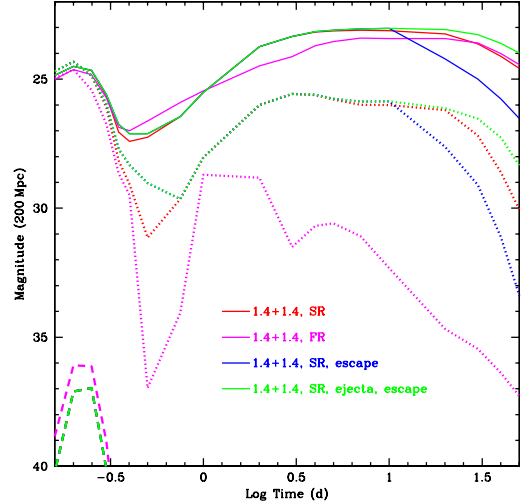


FIG. 15.— Magnitude versus time for the three models shown in Figure 14: standard model (red), reduced-gamma deposition model (blue), and the model with both reduced-gamma deposition and increased tidal ejecta mass (green). Additionally, a standard model with the fully relativistic opacity treatment is included (magenta). Emission from different wavelength bands are indicated by curves of the following types: IR (solid), nIR (dotted) and red-band optical (dashed).

from these ejecta used simplifications to the opacities, e.g. the expanding-opacity approximation based on the Sobolev method, that may not be valid for a macronova transient. Compared to the Doppler-broadened opacity method proposed here, expansion opacities are over an order of magnitude smaller. All of the atomic physics models considered in this work produce macronova luminosities that are shifted redward to infra-red bands and an order of magnitude dimmer compared to past calculations. Discrepancies appear in the details of the spectra arising from these models, such as the precise wavelength band in which an observable EM signal occurs, indicating some sensitivity to the atomic physics assumptions that should be considered in future studies. Simplifications associated with the morphology of the dynamic ejecta and radiation transport scheme applied in this work also warrant additional investigation.

These results have immediate repercussions for any follow-up searches for GW sources, arguing that infrared detectors are key. The primary caveat to this conclusion is that our study has focused exclusively on the dynamic ejecta of a neutron star merger. Being extremely neutron-rich and ejected at large velocities, these ejecta produce the “strong” r -process material ($A > 130$) for which we have calculated representative opacities in this paper. Matter that is exposed longer to the neutrino emission from the remnant, either in the form of neutrino-driven winds or accretion disk material that becomes unbound on a viscous time scale ($\sim 0.3 \text{ s}$), will, however, possess different properties: it will have lower velocities and larger electron fractions and therefore undergo a different nucleosynthesis. A number of recent studies (Wanajo et al. 2014; Perego et al. 2014; Just et al. 2015) found that compact binary mergers also eject a substantial amount of such matter with higher electron fractions. This material complements the dynamic ejecta with lower-mass

r -process ($A < 130$) and produces transients that are brighter and peak at shorter wavelengths (Kasen et al. 2015; Martin et al. 2015). One also has to seriously consider the possibility that the purported observations of macronovae, e.g. GRB 130603B (Tanvir et al. 2013; Berger et al. 2013) and GRB 060614 (Jin et al. 2015; Yang et al. 2015) had a different origin. Such solutions, however, have their own difficulties (Berger et al. 2013) and we leave the further exploration of the topic to future studies. Certainly the upper limits placed by GRB

150101B suggest that either the observations from GRB 130603B and GRB 060614 did not arise from macronovae or there is sufficient variability in the disk wind to produce a wide range of results (Fong et al. 2016).

This work was carried out under the auspices of the National Nuclear Security Administration of the US Department of Energy at Los Alamos National Laboratory and supported by contract no DE-AC52-06NA25396. Helpful discussions with O. Korobkin are gratefully acknowledged.

REFERENCES

- Abbott, B. P., Abbott, R., Abbott, T. D., et al. 2016a, *ApJ*, 818, L22
- . 2016b, *Physical Review Letters*, 116, 241103
- . 2016c, *Physical Review Letters*, 116, 061102
- Abdallah, J., R.E.H. Clark, & R.D. Cowan. 1988, Los Alamos Manual LA-11436-M, Vol. I
- Arnett, W. D., Fryer, C. L., & Matheson, T. 2016, *ArXiv e-prints*, arXiv:1611.08746
- Barnes, J., & Kasen, D. 2013, *ApJ*, 775, 18
- Barnes, J., Kasen, D., Wu, M.-R., & Martínez-Pinedo, G. 2016, *ApJ*, 829, 110
- Belczynski, K., Dominik, M., Bulik, T., et al. 2010, *ApJ*, 715, L138
- Berger, E. 2014, *ARA&A*, 52, 43
- Berger, E., Fong, W., & Chornock, R. 2013, *ApJ*, 774, L23
- Biémont, E., Palmeri, P., & Quinet, P. 1999, *Ap&SS*, 269, 635
- Biémont, E., Quinet, P., Svanberg, S., & Xu, H. L. 2004, *Journal of Physics B Atomic Molecular Physics*, 37, 1381
- Castor, J. L. 1974, *MNRAS*, 169, 279
- Colgan, J., Kilcrease, D. P., Magee, N. H., et al. 2016, *ApJ*, 817, 116
- Connaughton, V., Burns, E., Goldstein, A., et al. 2016, *ArXiv e-prints*, arXiv:1602.03920
- Cowan, R. D. 1981, *The theory of atomic structure and spectra* (Berkeley: University of California Press)
- Dominik, M., Berti, E., O’Shaughnessy, R., et al. 2015, *ApJ*, 806, 263
- Eastman, R. G., & Pinto, P. A. 1993, *ApJ*, 412, 731
- Eichler, D., Livio, M., Piran, T., & Schramm, D. N. 1989, *Nature*, 340, 126
- Fong, W., Berger, E., Margutti, R., & Zauderer, B. A. 2015, *ApJ*, 815, 102
- Fong, W., Berger, E., Margutti, R., et al. 2012, *ApJ*, 756, 189
- Fong, W., Berger, E., Metzger, B. D., et al. 2014, *ApJ*, 780, 118
- Fong, W., Margutti, R., Chornock, R., et al. 2016, *ApJ*, 833, 151
- Fontes, C. J., Colgan, J., & Abdallah Jr, J. 2016, in *Modern Methods in Collisional-Radiative Modeling of Plasmas*, ed. Y. Ralchenko (New York: Springer), 17
- Fontes, C. J., Fryer, C. L., Hungerford, A. L., et al. 2015a, *High Energy Density Physics*, 16, 53
- Fontes, C. J., Zhang, H. L., Abdallah, Jr., J., et al. 2015b, *Journal of Physics B Atomic Molecular Physics*, 48, 144014
- Fryer, C. L., Colgate, S. A., & Pinto, P. A. 1999, *ApJ*, 511, 885
- Ganapol, B. D., & Pomraning, G. C. 1987, *J. Quant. Spec. Radiat. Transf.*, 37, 297
- Greiner, J., Burgess, J. M., Savchenko, V., & Yu, H.-F. 2016, *ArXiv e-prints*, arXiv:1606.00314
- Grossman, D., Korobkin, O., Rosswog, S., & Piran, T. 2014, *MNRAS*, 439, 757
- Hakel, P., Sherrill, M. E., Mazevet, S., et al. 2006, *J. Quant. Spec. Radiat. Transf.*, 99, 265
- Hotokezaka, K., Wajajo, S., Tanaka, M., et al. 2016, *MNRAS*, 459, 35
- Huebner, W. F., & Barfield, W. D. 2014, *Astrophysics and Space Science Library*, Vol. 402, *Opacity* (New York: Springer), doi:10.1007/978-1-4614-8797-5
- Jin, Z.-P., Li, X., Cano, Z., et al. 2015, *ApJ*, 811, L22
- Just, O., Bauswein, A., Pulpillo, R. A., Goriely, S., & Janka, H.-T. 2015, *MNRAS*, 448, 541
- Karp, A. H., Lasher, G., Chan, K. L., & Salpeter, E. E. 1977, *ApJ*, 214, 161
- Kasen, D. 2006, *ApJ*, 649, 939
- Kasen, D., Badnell, N. R., & Barnes, J. 2013, *ApJ*, 774, 25
- Kasen, D., Fernández, R., & Metzger, B. D. 2015, *MNRAS*, 450, 1777
- Kasen, D., Thomas, R. C., & Nugent, P. 2006, *ApJ*, 651, 366
- Kohn, W., & Sham, L. J. 1965, *Physical Review*, 140, 1133
- Kouveliotou, C., Meegan, C. A., Fishman, G. J., et al. 1993, *ApJ*, 413, L101
- Kramida, A., Yu. Ralchenko, Reader, J., & and NIST ASD Team. 2015, *NIST Atomic Spectra Database* (ver. 5.3), [Online]. Available: <http://physics.nist.gov/asd> [2016, March 24]. National Institute of Standards and Technology, Gaithersburg, MD.
- Kulkarni, S. R. 2005, *ArXiv Astrophysics e-prints*, astro-ph/0510256
- Li, L.-X., & Paczyński, B. 1998, *ApJ*, 507, L59
- Lyutikov, M. 2016, *ArXiv e-prints*, arXiv:1602.07352
- Magee, N. H., Abdallah, J., Colgan, J., et al. 2004, in *American Institute of Physics Conference Series*, Vol. 730, American Institute of Physics Conference Series, ed. J. S. Cohen, D. P. Kilcrease, & S. Mazavet (New York: AIP), 168
- Martin, D., Perego, A., Arcones, A., et al. 2015, *ApJ*, 813, 2
- Metzger, B. D., Martínez-Pinedo, G., Darbha, S., et al. 2010, *MNRAS*, 406, 2650
- Palmeri, P., Quinet, P., Wyart, J.-F., & Biémont, E. 2000, *Phys. Scr*, 61, 323
- Perego, A., Rosswog, S., Cabezon, R. M., et al. 2014, *MNRAS*, 443, 3134
- Pinto, P. A., & Eastman, R. G. 2000, *ApJ*, 530, 757
- Pomraning, G. C. 1971, *J. Quant. Spec. Radiat. Transf.*, 11, 597
- Quinet, P., & Biémont, E. 2004, *Atomic Data and Nuclear Data Tables*, 87, 207
- Quinet, P., Palmeri, P., & Biémont, E. 1999, *J. Quant. Spec. Radiat. Transf.*, 62, 625
- Rosswog, S., Korobkin, O., Arcones, A., Thielemann, F.-K., & Piran, T. 2014, *MNRAS*, 439, 744
- Sampson, D. H., Zhang, H. L., & Fontes, C. J. 2009, *Phys. Rep.*, 477, 111
- Sobolev, V. V. 1960, *Moving envelopes of stars* (Cambridge: Harvard University Press)
- Tanaka, M., & Hotokezaka, K. 2013, *ApJ*, 775, 113
- Tanvir, N. R., Levan, A. J., Fruchter, A. S., et al. 2013, *Nature*, 500, 547
- van Rossum, D. R., Kashyap, R., Fisher, R., et al. 2016, *ApJ*, 827, 128
- Wajajo, S., Sekiguchi, Y., Nishimura, N., et al. 2014, *ApJ*, 789, L39
- Wollaeger, R. T., & van Rossum, D. R. 2014, *ApJS*, 214, 28
- Yang, B., Jin, Z.-P., Li, X., et al. 2015, *Nature Communications*, 6, 7323